# Excitation gratings in cross-beam filament wake channels in a dense argon gas: Formation, control, and Rabi sideband manifestation

Suyash Bajpai <sup>1</sup> and Dmitri A. Romanov <sup>1,2</sup>

<sup>1</sup>Department of Physics, Temple University, Philadelphia, Pennsylvania 19122, USA

<sup>2</sup>Center for Advanced Photonics Research, College of Science and Technology, Temple University, Philadelphia, Pennsylvania 19122, USA



(Received 1 February 2023; accepted 5 May 2023; published 5 June 2023)

When two intense laser beams cross at a small angle, the interference in the crossing area results in a finite intensity grating. We consider femtosecond laser filamentation in such a grating, in a situation when the process is largely confined to the grating maxima and leads to formation of a structured filament wake channel. In a dense gas, electron impact processes during the laser pulse cause a copious excitation of neutral atoms, resulting in formation of a finite grating of the density of excited atoms. Numerically solving the equations of laser-driven kinetics, we obtain the properties of this grating, as depending on the characteristics of the interfering beams and especially on the interbeam phase delay. The excitation gratings thus formed give rise to a hallmark effect of Rabi sideband emission when probed by a picosecond 800 nm laser pulse, which couples with transitions in the excited states manifold. Spectral and spatial interference of the emitted radiation forms four-dimensional spatial-spectral fringe patterns accessible for observation on a remote screen. The patterns are indicative of the excitation grating structure; their sensitivity to the phase delay between the crossing pump pulses warrants experimental verification.

## DOI: 10.1103/PhysRevE.107.065202

#### I. INTRODUCTION

Filamentation of intense femtosecond laser pulses in gases and its applications have been a center of growing attraction over the past three decades. Potential applications include guiding electric discharges, atmospheric monitoring through LIDAR (light detection and ranging; the technique utilizes white light continuum generation by a filament to achieve full spectral coverage in a single shot), terahertz generation, etc. [1–4]. The filamentation process is initiated when an intense laser pulse self-focuses in a nonlinear medium, until it reaches high enough intensity to ionize the gas in its path, thus leaving behind a narrow column of plasma. This plasma formation evolves in the pulse wake and is open to various pump-probe experiments [5-8].

Depending on experimental settings, a multifilament system may emerge [9], leading to a structured wake channel of considerable complexity. One convenient way of eliciting a controllable structured filamentation is to use two identical laser beams crossing at a small angle and producing an interference pattern. Similar arrangements with cw laser beams have been utilized for various purposes since the 1970s [10]. With ultrashort pulses, transient polarization gratings at the beam crossing were widely used as means for degenerate four-wave mixing [11-13]. More recently, electron-density gratings generated in this setting in the strong-field regime have attracted considerable attention. There have been studies of such gratings induced either by the ponderomotive force [14,15] or by spatial variations of the ionization rate [16–19], conducted with IR lasers and also with UV lasers [20]. The dynamic electron-density gratings were shown to cause effective energy transfer between filamenting beams that slightly

differ in carrier frequency [21–23]. Electron energy gratings in quasineutral plasma generated by two counterpropagating laser beams have been studied extensively, both theoretically and experimentally, in relation to controlled fusion applications [24–27].

In contrast to these studies, we are interested in the density grating of excited argon atoms, as the massive production of exited atoms is a salient feature of filamentation in a dense gas [8,28]. When the interatomic distances are comparable or smaller than the amplitude of the free electron excursions in the oscillating laser field, the electrons released by ionization undergo multiple collisions with neighboring neutral atoms during the laser pulse, and these collisions largely determine the energy intake by the medium. In particular, the collisional processes result in considerable buildup of the excited atoms' concentration. We will consider this hallmark effect in the case of a high-pressure argon gas interacting with an intense femtosecond pulse of the standard 800 nm carrier wavelength.

The collisional effects, in which the free electrons are engaged in this case, can be broken down to the energy gain by the inverse bremsstrahlung caused by elastic scattering on neutral atoms, and to the energy-loss effects of impact ionization and collisional excitation. These two latter effects compete during the laser pulse, and this competition allows for pulse-shape control of the resulting excited-atom and ionic densities [29]. The impact ionization rate is a steeper function of energy, but it has a later onset, so there is an energy range in which the collisional excitation dominates, and this range has to be passed by the electrons as they climb up the energy scale. This leads to considerable buildup of the density of excited atoms throughout the laser pulse. By the end of the laser pulse, a grating structure of excited-atom density emerges in the

crossing area of the two beams. The enhanced laser intensity in the interference maxima allows for both the strong-field ionization and the collisional processes to be confined within the intensity grating lines in the crossing region, thus making for an excitation grating of finite length and width, whose properties are controlled by the crossing angle and the phase difference between the two pulses.

In the pulse wake, this transient excited-atom grating can manifest itself in various linear and nonlinear optical effects. One hallmark nonlinear optical effect is the generation of giant Rabi sidebands, when an excited gas is probed by a moderately intense picosecond laser pulse [30,31]. When a suitable pair of excited states is coupled with the laser field, Rabi cycling occurs. The associated induced electric dipole oscillations produce sideband radiation at frequencies both redshifted and blueshifted about the carrier frequency of the driving laser pulse. An obvious condition for the sideband emission is the presence of occupied states with transition frequencies close to the laser frequency. The excited states' manifold of argon meets this condition, as related to the standard 800 nm carrier wavelength (another well-studied case is atomic oxygen), and indeed, Rabi sideband radiation from filament wake channels in argon and oxygen gases has been observed [30,31]. The emitted coherent broadband radiation is engaged in spectral interference, resulting in characteristic spatial-spectral fringe patterns controlled by the envelope shape of the probe pulse [32,33]. It may well be expected that when a probe pulse interacts with excited argon atoms in a finite grating formation, a sophisticated spatial-spectral interference pattern will result that will carry information of both the state of excitation and the spatial characteristics of the grating.

In this paper, we analyze theoretically the transient grating patterns of excited-atom density that forms during filamentation in a beam-crossing area in a dense argon gas and can be controlled by the crossing angle and the phase difference between the two pulses. Further, we study the Rabi sideband emission from the excitation gratings, which makes for characteristic spatial-spectral interference patterns when observed on a distant screen. We determine the dependence

of the interference spot positions on the characteristics of the excitation grating and ultimately on the characteristics of the crossing-beam pump pulses. To emphasize the control effects, we concentrate on the finite gratings that have a small number of grating lines within the laser beam diameter.

The text is organized as follows. In Sec. II, we explore the interference patterns in the two-beam crossing area, which depend on the crossing angle and the relative phase delay of the two pulses, and which form finite transient intensity gratings modulated by the beam profiles. In Sec. III, we analyze the buildup of atomic excitation in the high-intensity regions, which leads to a gratinglike distribution of excited atoms in the pulse wake. In Sec. IV, we investigate the Rabi sideband emission associated with the excited argon atoms in the grating and the resulting spatial-spectral interference patterns, and discuss the possible use of these patterns for determining the grating characteristics. Finally, in Sec. V, we put forward our conclusions.

### II. TRANSIENT INTENSITY GRATING

We consider two laser beams crossing at a small angle  $2\theta$ . The beams are linearly polarized with the polarization vector  $\hat{\mathbf{e}}$ being orthogonal to the crossing plane. The electric field in the two pulses is  $\mathbf{E}_1(\mathbf{r},t) = \hat{\mathbf{e}}\tilde{E}_1(\mathbf{r},t) \exp(ik\hat{\mathbf{k}}_1\mathbf{r} - i\omega_c t - i\varphi/2)$ and  $\mathbf{E}_2(\mathbf{r},t) = \hat{\mathbf{e}}\tilde{E}_2(\mathbf{r},t) \times \exp(ik\hat{\mathbf{k}}_2\mathbf{r} - i\omega_c t + i\varphi/2)$ , where  $\omega_c$  is the carrier frequency and  $k_c = \omega_c n_r/c$  is the wavevector magnitude,  $n_r = n_r(\omega_c)$  being the refractive index. The amplitudes  $\tilde{E}_1(\mathbf{r},t)$  and  $\tilde{E}_2(\mathbf{r},t)$  are slowly varying envelope functions, and  $\varphi$  is the phase delay between the pulses. The cycle-averaged intensity in the intersection region is  $I(\mathbf{r}, t) =$  $(\mu/2)\{|\tilde{E}_1|^2 + |\tilde{E}_2|^2 + 2\tilde{E}_1\tilde{E}_2\cos[k_c(\hat{\mathbf{k}}_1 - \hat{\mathbf{k}}_2)\mathbf{r} + \varphi]\}, \text{ where}$  $\mu = c n_r \varepsilon_0$  and  $\varepsilon_0$  is the vacuum permittivity. We assume that the two laser pulses have identical Gaussian radial shapes with the beam radius R, and identical Gaussian temporal envelope shapes with the pulse duration  $\tau$ ; we assign the Cartesian coordinate axes so that the beam-crossing plane is the xz plane and the z axis is the bisectrix of the beam crossing angle  $2\theta$ . Then,  $\hat{\mathbf{k}}_1 \mathbf{r} = \sin \theta x + \cos \theta z$  and  $\hat{\mathbf{k}}_2 \mathbf{r} = -\sin \theta x + \cos \theta z$ , so that

$$\tilde{E}_{1,2}(x, y, z, t) = E_0 \exp(-[(x\cos\theta \mp z\sin\theta)^2 + y^2]/R^2) \exp(-\{\pm\sin\theta x + \cos\theta z - v_g[t \mp \varphi/(2\omega_c)]\}^2/(\tau v_g)^2),$$
 (1)

where  $v_g = v_g(\omega_c) \approx c/n_r$  is the group velocity. This spatial and temporal dependence of the envelope functions makes, after some algebra, for the transient intensity grating in the form

$$I(\mathbf{r},t) = \mu E_0^2 \exp\left[-\frac{2}{R^2} (z^2 \sin^2\theta + x^2 \cos^2\theta + y^2)\right] \exp\left(-\frac{2}{(\omega_c \tau)^2} \left[(\omega_c t - k_c \cos\theta z)^2 + \frac{1}{4} (2k_c \sin\theta x + \varphi)^2\right]\right)$$

$$\times \left(\cosh\left[\frac{2}{(\omega_c \tau)^2} (\omega_c t - k_c \cos\theta z)(2k_c \sin\theta x + \varphi) + \frac{2}{R^2} \sin(2\theta)xz\right] + \cos(2k_c \sin\theta x + \varphi)\right). \tag{2}$$

As seen in Eq. (2), the transient intensity grating emerges as a rather complicated function of x, z, and t, while keeping a simple Gaussian shape in the direction orthogonal to the crossing plane (the y axis). The extent of the grating area is determined by the exponential in the first line of Eq. (1): the size of the finite grating along the x axis is about  $R/\cos\theta$  and along the z axis, about  $R/\sin\theta$ . There is also an additional

length scale determined by the exponential in the second line of Eq. (1):  $\omega_c \tau/(k_c \cos \theta) = c\tau/(n_r \cos \theta)$  along the z axis and  $\omega_c \tau/(k_c \sin \theta) = c\tau/(n_r \sin \theta)$  along the x axis. The kinematics of the intensity grating pattern is determined by the relative magnitude of the two z-axis scales. If  $c\tau/(n_r \cos \theta) > R/\sin \theta$ , that is,  $c\tau \tan \theta > n_r R$ , the intensity rises and falls in the grating area as a whole. If  $c\tau/(n_r \cos \theta) < R/\sin \theta$ , that

is,  $c\tau \tan \theta < n_r R$ , the transient intensity grating emerges at one end of the crossing region, then moves as a formation of the  $c\tau/(n_r \cos \theta)$  length along the z axis, and then disappears at the other end of the crossing region. For a typical pulse duration of 50 fs,  $c\tau/n_r \sim 15 \, \mu m$ , which for small values of the crossing angle  $\theta$  is smaller than  $R/\tan \theta$ , so that the second scenario is realized.

The grating modulation of the transient intensity pattern is mainly delivered by the last term in the third line of Eq. (2),  $\cos(2k_c\sin\theta x + \varphi)$ , which determines the grating fringe separation of  $\pi/(k_c \sin \theta)$ . However, the preceding exponential factors in the first and the second lines of Eq. (1) lead to slight modification of this period and a little shift of the grating pattern on the order of  $(k_c R \tan \theta)$ . Unlike these minor modifications, the interpulse phase delay  $\varphi$  plays a crucial role in controlling the intensity pattern and its resulting action on the medium. The intensity values at the maxima of the fringe pattern near the center of the crossing area are about four times greater than those in each of the beams; only a very finite number of the grating maxima that are close to this center will result in lasting effects on the medium, because of extreme nonlinearity of the laser-medium interaction. A change in the value of  $\varphi$  causes the grating modulation pattern to shift along the x axis and thus can change the number of highintensity grating lines. To illustrate this effect, we consider the intensity pattern determined by Eq. (2) at t = 0 and with z = y = 0. Modification of this pattern in response to changes

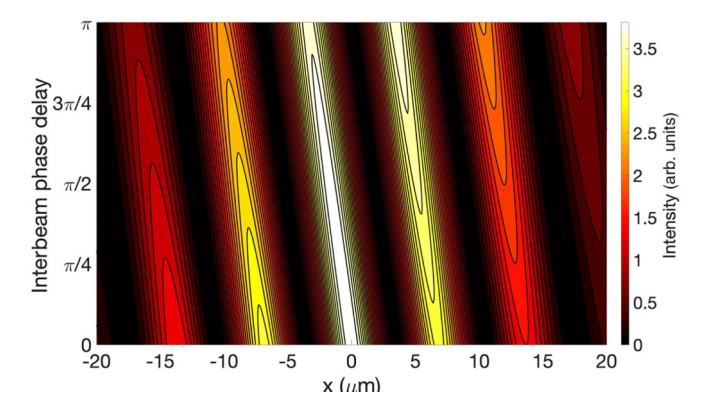


FIG. 1. Variation of the transient intensity grating in the crossing area of two identical laser beams caused by variation in the interbeam phase delay. Both laser pulses have a beam radius of  $R=10~\mu m$  and a duration of 50 fs; the crossing angle  $\theta=0.057~\rm rad$ . The shown grating corresponds to t=0 and z=0 in Eq. (2).

in the interbeam phase delay is presented in Fig. 1. Here, both laser pulses have a beam radius of  $R = 10 \,\mu\text{m}$  and a duration of 50 fs, while the crossing angle is  $\theta = 0.057 \,\text{rad}$ , which corresponds to the intensity grating separation of  $d = 7 \,\mu\text{m}$  (the value of d comparable to R is chosen to emphasize the finite grating effects). The positions of the maxima  $x_M$  of this function I(x) are found as the roots of the equation,

$$\tan\left(k_c\sin\theta x_M + \frac{\varphi}{2}\right) = \frac{\varphi}{\left(k_c R \tan\theta\right)^2} - 2k_c\sin\theta x_M \left[\frac{1}{\left(k_c R \tan\theta\right)^2} + \frac{1}{\left(\omega_c \tau\right)^2}\right]. \tag{3}$$

In a typical case, the right-hand side in this equation brings about small corrections responsible for the slight deviations mentioned in the previous paragraph. For a given maximum  $x_M$ , the shift of interbeam phase delay by  $\Delta \varphi$  causes the shift

$$\Delta x_M = -\frac{\Delta \varphi}{2k_c \sin \theta} \left( 1 - \left\{ (k_c R \tan \theta)^2 + \frac{1}{(k_c R \tan \theta)^2} [\varphi Q + 2k_c \sin \theta x_M (1 + Q)]^2 + 2(1 + Q) \right\}^{-1} \right), \tag{4}$$

where  $Q = (k_c R \tan \theta)^2 / (\omega_c \tau)^2 = (n_r R \tan \theta)^2 / (c\tau)^2$ .

As the strong-field effects on the gas are extremely nonlinear, this difference in intensity easily leads to a situation when the ionization and atomic excitation in the gas medium in the pulse wake are confined to the crossing area and virtually absent outside that region. We use this spatiotemporal form of the localized transient intensity grating of Eq. (2) as the input in the equations that describe the kinetics of the electronic degrees of freedom during the pulse, with the emphasis on the production of excited atoms as a hallmark of the dense gas situation.

# III. FORMATION OF AN EXCITATION GRATING DURING THE LASER PULSE

As mentioned in the Introduction, in a relatively dense gas collisional processes lead to a heavy presence of excited atoms in the immediate wake of the laser pulse. These excited atoms are produced by collisional excitation performed by energetic free electrons driven by the oscillating electric field. In turn, the dominant part of these free electrons results from impact

ionization of argon atoms by the field-driven electrons as well. Moreover, in the dense-gas situation, the possible shift of the free electrons away from the intensity maxima by the action of ponderomotive force can be neglected, because this force becomes effectively screened and does not lead to a noticeable charge separation and deviations from electrical neutrality of the emerging plasma.

During the laser pulse, the emerging free electrons become immediately engaged in three field-driven impact processes: (i) energy gain via inverse bremsstrahlung on neutral neighbors; (ii) collisional excitation of neutral atoms, which is associated with energy loss by the free electrons; and (iii) impact ionization, which is associated with both the energy loss by free electrons and the generation of new free electrons. The two later processes compete between themselves for the energy that the electronic system receives from the laser field in the first process.

Strictly speaking, there are several accessible excited atomic states, each corresponding to a separate density function and separate excitation rate. However, we will restrict our model with one representative excited state, which has the excitation energy of  $\varepsilon_{ex} = 11.8 \text{ eV}$  and the evolving density of excited atoms  $n_{ex}(\mathbf{r},t)$ . We follow the model outlined in Refs. [28,34] and describe the laser-driven kinetics of free electrons in terms of the local density of free-electron occupied energy states,  $n(\mathbf{r}, \varepsilon, t)$ . Then, the evolution of  $n_{\rm ex}(\mathbf{r}, t)$  is expressed in terms of  $n(\mathbf{r}, \varepsilon, t)$  and the excitation rate  $v_{ex}(\varepsilon)$ . Using the semiempirical formula of Ref. [35] for the cumulative excitation cross section, the effective excitation rate is expressed as  $v_{\rm ex}(\varepsilon) = v_{\rm ex0} f_{\rm ex}(\varepsilon/\varepsilon_{\rm ex})$ . Here, the dimensional factor is  $v_{\rm ex0} = 1.35 n_0 \pi a_B^2 ({\rm Ry}/\varepsilon_{\rm ex})^2 \sqrt{2\varepsilon_{\rm ex}/m}$ , where  $n_0$  is the density of neutral atoms (we will neglect the depletion of the neutral-atom population),  $a_B$  is the Bohr's radius, Ry is the Rydberg energy, and m is the electron mass; the dimensionless function is  $f_{\text{ex}}(z) = (1/z)^{0.25} (1 - 1/z)^2 \Theta(z - 1)$ . The evolution of  $\varepsilon = \varepsilon_{\rm ex}$  during the pulse is expressed as

$$\frac{dn_{\rm ex}}{dt} = \nu_{\rm ex0} \int_0^\infty d\varepsilon f_{\rm ex}(\varepsilon/\varepsilon_{\rm ex}) n(\mathbf{r}, \varepsilon, t). \tag{5}$$

In turn, the electrons that perform the collisional excitation emerge in two ways: a minor part of them is created by the strong-field ionization of argon atoms with the atomic ionization rate,  $W(\mathbf{r},t)$ . The exact form of  $W(\mathbf{r},t)$  is of little importance, as these primary electrons merely serve as a seed for the impact ionization. Thus, it suffices to use a convenient approximation for  $W(\mathbf{r},t)$ . For the laser intensities of  $\sim 10^{14} \,\mathrm{W/cm^2}$  at the maxima of the intensity grating fringes, the value of the Keldysh parameter  $\gamma$  for argon atoms is about 1.15. It was shown [36,37] that the ADK formula [38] still gives a reasonably good approximation for  $W(\mathbf{r},t)$  for the borderline values of  $\gamma$  slightly greater than unity, and so we use it here. The second, major source of free electrons is the impact ionization process, the energy-dependent rate of which,  $v_{ion}(\varepsilon)$ , is obtained using the semiempirical Lotz formula for the total ionization cross section [39]. For Ar and the electron energies in question,  $\nu_{\rm ion}(\varepsilon) = 3.63 \nu_{\rm ex0} (\varepsilon_{\rm ex}/\varepsilon_{\rm ion})^{3/2} f_{\rm ion}(\varepsilon/\varepsilon_{\rm ion}), \text{ where } f_{\rm ion}(z) =$  $\sqrt{1/z}\{1-0.62 \exp[-0.40(z-1)]\} \ln(z)\Theta(z-1)$ . Overall, the total number of free electrons grows with the rate  $(dn_i/dt) = n_0 W(\mathbf{r}, t) + \int_0^\infty d\varepsilon \nu_{\rm ion}(\varepsilon) n(\mathbf{r}, \varepsilon, t)$ . Finally, the function  $n(\mathbf{r}, \varepsilon, t)$  is also determined by the ionization and excitation processes, as well as by the energy intake and redistribution via inverse bremsstrahlung:

$$\frac{\partial n}{\partial t} = \left. \frac{\partial n}{\partial t} \right|_{\text{ex}} + \left. \frac{\partial n}{\partial t} \right|_{\text{ion}} + \left. \frac{\partial n}{\partial t} \right|_{\text{B}}.$$
 (6)

The collisional excitation in Eq. (5) is performed by the free electrons at the expense of the kinetic energy loss. As a result, the free electrons are reshuffled along the energy axis via finite energy shifts, so that

$$\frac{\partial n}{\partial t}\Big|_{\text{ex}} = \int_0^\infty d\varepsilon' [-\delta(\varepsilon' - \varepsilon) + \delta(\varepsilon' - \varepsilon - \varepsilon_{ex})] \\
\times \nu_{\text{ex}}(\varepsilon') n(\mathbf{r}, \varepsilon', t).$$
(7)

The impact ionization affects  $n(\mathbf{r}, \varepsilon, t)$  in a similar way; besides, it constantly supplies new electrons, contributing to  $(dn_i/dt)$  along with the strong-field ionization. These new electrons emerge with low kinetic energy, but upon the first cycle of laser-field acceleration and elastic scatter-

ing, which is beyond our model framework, they acquire some initial energy distribution, which is accounted for by an auxiliary function  $g(\varepsilon)$ . The specific form of this seed function is of no particular importance; we choose  $g(\varepsilon) = C_{k\eta} \varepsilon^k \{1 - \tanh[\eta(\varepsilon - U_p)]\}$ , where k and  $\eta$  are adjustable parameters,  $U_p$  is the ponderomotive energy, and  $C_{k\eta}$  is the normalization constant. Thus, the second term on the right-hand side of Eq. (6), which expresses the effects of impact ionization, reads

$$\frac{\partial n}{\partial t}\Big|_{\text{ion}} = \int_{0}^{\infty} d\varepsilon' [-\delta(\varepsilon' - \varepsilon) + \delta(\varepsilon' - \varepsilon - \varepsilon_{\text{ion}})] \times \nu_{\text{ion}}(\varepsilon') n(\mathbf{r}, \varepsilon', t) + g(\varepsilon) \frac{dn_{i}}{dt}.$$
(8)

The last term on the right-hand side of Eq. (6) represents the transformation of  $n(\mathbf{r}, \varepsilon, t)$  due to the inverse bremsstrahlung on neutral atoms. Assuming the laser carrier frequency to be greater than the scattering rate of an electron on neutral atoms, which in turn is greater than the inverse of the pulse duration, this term is obtained [28] as

$$\left. \frac{\partial n}{\partial t} \right|_{B} = \frac{e^{2}}{3\mu m \omega_{c}^{2}} \sqrt{\frac{2}{m}} n_{0} \sigma_{tr}(\varepsilon) I(\mathbf{r}, t) \frac{\partial}{\partial \varepsilon} \left[ \sqrt{\varepsilon} \left( \varepsilon \frac{\partial n}{\partial \varepsilon} - \frac{1}{2} n \right) \right],$$
(9)

where  $I(\mathbf{r}, t)$  is the transient intensity grating described in the preceding section, and  $\sigma_{tr}(\varepsilon)$  is the cross section for elastic scattering. This Fokker-Planck-type term describes the effective diffusion of the electron density along the energy axis, with the time-dependent diffusion coefficient [40].

The outcomes of the competition between the impact ionization and collisional excitation are determined by the energy-dependent rates of these processes,  $\nu_{\rm ion}(\varepsilon)$  and  $\nu_{\rm ex}(\varepsilon)$ . (The elastic-scattering cross section can be considered virtually constant in the relevant energy range 5–20 eV:  $\sigma_{tr}(\varepsilon) \approx$  $\sigma_0 = 10^{-15} \,\mathrm{cm}^2$ , as this range lies well away from the Ramsauer minimum [41].) Since  $v_{\rm ex}(\varepsilon)$  has its inception point at a smaller value of energy than that for  $v_{ion}(\varepsilon)$ , there is an energy interval in which  $v_{\rm ex}(\varepsilon) > v_{\rm ion}(\varepsilon)$ . When the electrons climb up the energy axis, they inevitably enter this region, and thus impact ionization is necessarily accompanied by collisional excitation. The relative outcome of these two processes is determined by the details of the field-driven electron dynamics during the pulse, and may be modified by changes in the temporal shape of the pulse envelope [29]. When driven by the transient intesity grating in the beam-crossing area, the discussed processes duly produce gratinglike spatial distributions of the free electrons  $n(\mathbf{r}, t)$ , the ions  $n_i(\mathbf{r}, t)$ , and the excited atoms  $n_{\rm ex}({\bf r},t)$ . We are particularly concerned with the grating of  $n_{\rm ex}({\bf r},t)$  as it is a hallmark of a dense-gas situation.

We have solved numerically Eq. (6) for  $n(\mathbf{r}, \varepsilon, t)$  and obtained the buildup evolution of the excited-atom density  $n_{\rm ex}(\mathbf{r},t)$  as caused by the transient intensity grating in the beam-crossing area discussed in the previous section. The argon gas is at 60 atm pressure, which is the same as reported in the experiment of Ref. [8]. This corresponds to the gas density of  $1.8 \times 10^{21} \, \mathrm{cm}^{-3}$ . The parameters of the laser pulses in the two crossing beams are the same as those presented in Fig. 1. The pulses have the same carrier wavelength of 800 nm, the identical Gaussian transverse spatial shape with

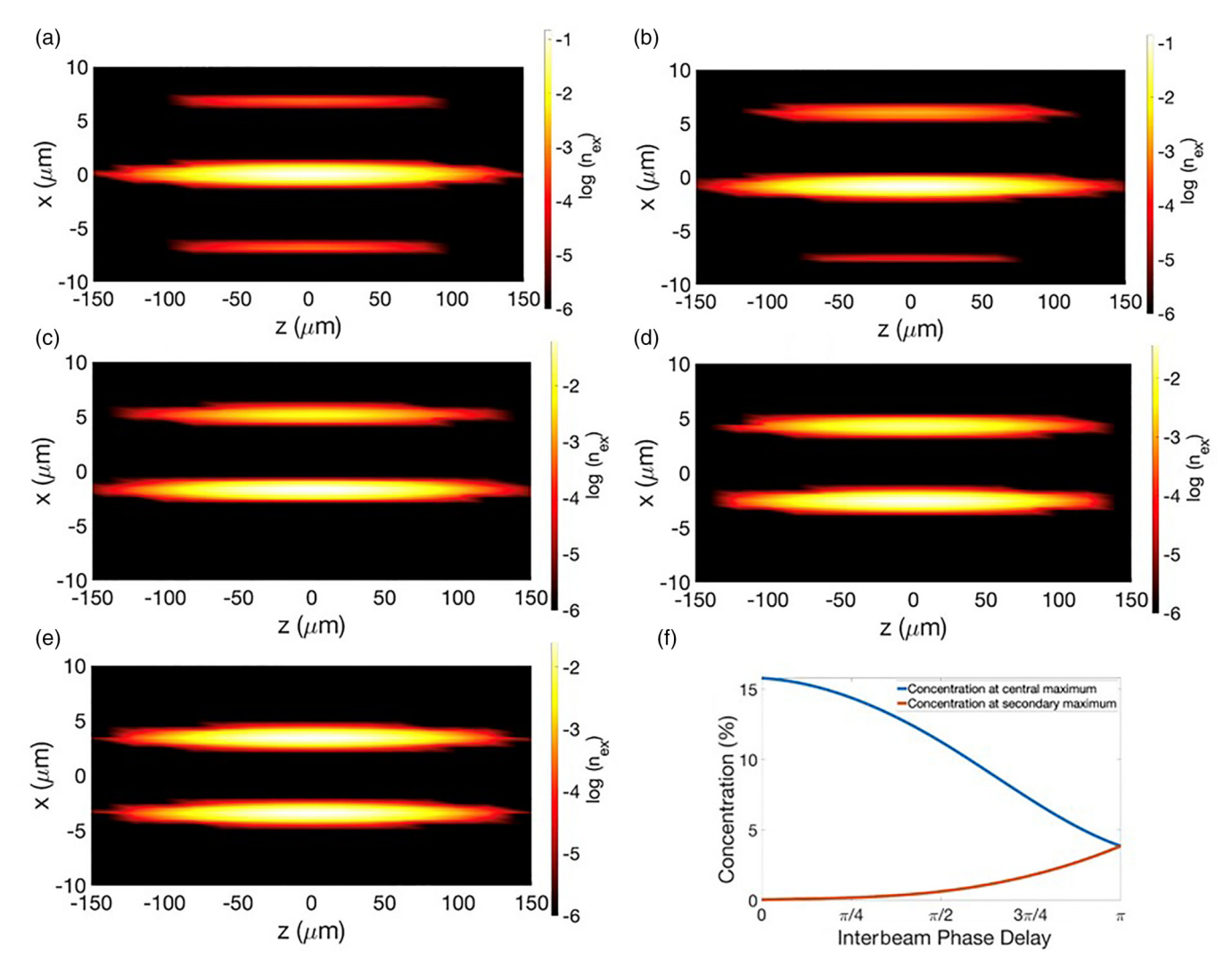


FIG. 2. Spatial distributions of the excited-atom concentration at the end of the laser pulse in the beam-crossing area for the crossing angle  $\theta=0.057$  rad and different values of the interpulse phase delay: (a)  $\varphi=0$ ; (b)  $\varphi=\pi/4$ ; (c)  $\varphi=\pi/2$ ; (d)  $\varphi=3\pi/4$ ; (e)  $\varphi=\pi$ . (Note the vastly different scales along the z axis and the x axis).

the beam radius  $R = 10 \,\mu\text{m}$ , the Gaussian temporal envelope shape with the pulse duration of  $\tau = 50$  fs, and the intensity of  $2.8 \times 10^{13} \,\mathrm{W/cm^2}$ . Assuming the transient intensity gratings as expressed by Eq. (2), we have found the distributions of excited atoms and ions at the end of the laser pulse. The characteristics of the obtained excitation grating patterns are determined both by the underlying laser intensity grating and the interplaying ionization-excitation processes during the pulse. Several representative examples of the obtained excitation gratings are shown in Fig. 2. These five characteristic grating patterns correspond to the beam-crossing angle of  $\theta =$ 0.057 rad and a few different values of the interpulse phase delay  $\varphi$ . The chosen value of the crossing angle corresponds to the intensity grating separation,  $d = 7 \,\mu\text{m}$ . As seen in Fig. 2, in all five cases the concentration of excited atoms reaches maximum at the positions on the grating lines that are closest to the center of the pattern (the point with coordinates x = 0, z = 0). Away from the center, the concentration decreases in both directions, although this decline is much faster in the x direction as compared to the z direction. The interbeam

phase delay has a prominent effect on the structure of the excitation grating, The zero phase delay,  $\varphi = 0$ , corresponds to the concentration grating pattern having a maximum right on the z axis [Fig. 2(a)]. This central maximum is accompanied by two weaker secondary maxima. The phase delay of  $\varphi = \pi$  corresponds to the pattern having a minimum on the z axis [Fig. 2(e)]. In this case, the pattern has two equally pronounced global maxima. (Actually, in this latter case, due to corrections to the positions of intensity grating lines determined by Eq. (2) and discussed in the previous section, the grating having a minimum on the z axis corresponds to a slightly different value of  $\varphi = 1.005 \pi$ ; we refer to it as  $\varphi = \pi$  for the sake of simplicity.) In both these limiting cases, at  $\varphi = 0$  and  $\varphi = \pi$ , the obtained grating patterns possess mirror symmetry along both the x axis and the z axis. For the intermediate values of the phase delay,  $\varphi = \pi/4$ ,  $\varphi = \pi/2$ , and  $\varphi = 3\pi/4$ , the mirror symmetry along the x axis is lifted. When the value of  $\varphi$  if increased from  $\varphi = 0$  to  $\varphi = \pi/4$ , the grating shifts in the (-x) direction and also starts showing an increase in the concentration at the secondary maximum

lying in the (+x) direction and a decrease in the concentration at the secondary maximum in the (-x) direction [Fig. 2(b)]. Further increase in  $\varphi$  to  $\varphi = \pi/2$  leads to further increase in the (+x) maximum, while the (-x) maximum virtually disappears [Fig. 2(c)]. When the interbeam phase delay further increases to  $\varphi = 3\pi/4$ , the remaining (+x) secondary maximum gains even more concentration and becomes comparable with the main maximum [Fig. 2(d)]. Eventually, at  $\varphi = \pi$ , the values of the two maxima become indistinguishable, which restores the mirror symmetry along the x axis [Fig. 2(e)]. The absolute values of the excited-atom concentration at these two maxima are plotted as functions of  $\varphi$  in Fig. 2(f). As seen in this panel, the excited-atom concentration at the initially central maximum decreases with the increase in the phase delay. On the other hand, the concentration at a secondary maximum [(-x) fringe] grows steadily with the phase delay. Eventually, at  $\varphi = \pi$ , the two concentrations become equal.

The ionization gratings are similar in shape and behavior to the excitation gratings, albeit the values of ion concentration at the maxima of the fringes is smaller than those of the excited-atom concentrations; the ratio of the excited-atom concentration to the ion concentration can be further controlled by the envelope shape of the laser pulses [29].

# IV. RABI SIDEBAND GENERATION FROM THE EXCITATION GRATING

The excited states of Ar that are populated during the laser pulse as described in the preceding section relate to several noticeable fluorescence lines that lie conveniently close to the typical laser carrier wavelength of 800 nm: 811.5311, 810.3693, 801.4786, 800.6157, and 794.8176 nm [42]. Each of these transitions can couple to the 800 nm laser radiation as an effective two-state system. When such a system is driven by the oscillating electric field of a moderately intense probe laser pulse,  $\mathbf{E}_p(t) = \mathbf{\hat{e}}\tilde{E}_p(t) \exp(-i\omega_c t)$ , the Rabi oscillations occur, with the time-dependent induced dipole [43],

$$\mu(t) = \mu_{ab} \frac{\Omega(t)}{\Omega'(t)} \left( \cos(\omega_c t) - \frac{1}{2} \left\{ \left[ 1 + \frac{\Delta}{\Omega'(t)} \right] \cos \left[ \omega_c t - \int_0^t dt' \Omega'(t') \right] - \left[ 1 - \frac{\Delta}{\Omega'(t)} \right] \cos \left[ \omega_c t + \int_0^t dt' \Omega'(t') \right] \right\} \right). \quad (10)$$

Here,  $\mu_{ab}$  is the transition dipole matrix element,  $\Omega(t) = \mu_{ab}\tilde{E}_p(t)/\hbar$  is the instantaneous Rabi frequency,  $\Omega'(t) = \sqrt{\Delta^2 + \Omega^2(t)}$  is the instantaneous generalized Rabi frequency, and  $\Delta = \omega_{ba} - \omega_c$  is the detuning from the resonance. The two terms in the second line of Eq. (10) give rise to the redshifted and blueshifted Rabi sidebands, respectively, in the dipole-emitted radiation, as they correspond to instantaneous frequencies,  $\omega_{\pm}(t) = \omega_c \pm \Omega'(t)$ . As the value of  $\Omega'(t)$  varies during the laser pulse, first increasing to some maximum value and then decreasing back to zero, broad sidebands in the emission spectrum result.

Moreover, during the laser pulse, each available value of  $\Omega'$  occurs twice: at the leading ramp of the pulse and at the trailing ramp. The pairs of emitted same-frequency waves interfere, depending on the phase accumulation between their emission times. This spectral interference results in the characteristic fringe patterns of the sideband spectra, which are determined by the envelope shape or the probe pulse [33,44]. Formally, these spectral fringe patterns are obtained via Fourier transform of the induced dipole oscillations in Eq. (10).

When contributed by a large number of excited atoms in a filament wake channel, the sideband radiation bears an imprint of the spatial distribution of these coherent emitters and depends also on the transverse intensity profile of the probe beam. The interference of the waves emitted by the induced dipoles at different locations combines with the spectral interference and leads eventually to a characteristic spatial-spectral pattern, in which the fringes depend both on the frequency (or wavelength) and on the position on the observation screen [32]. In addition to this, in argon the spatial-spectral interference patterns to be observed will be contributed by the Rabi sidebands associated with all of the five above-mentioned transitions.

We simulated the spatial-spectral interference patterns of Rabi sidebands that can be observed when the excitation grating in Ar obtained in the preceding section is probed by a moderately intense picosecond 800 nm laser pulse. The probe beam is incident normally on the xz grating plane, with the beam axis (y) going through the center of the grating [the (0,0)point in the xz plane; see Sec. IIII. The sideband emission from the grating lines forms characteristic spatial-spectral patterns at a distant observation screen, which is parallel to the grating plane and is placed 20 cm away from the grating, to allow the interference fringes to gain the spatial scale in the cm range. Overall, the intensity of the observed signal depends on three variables: the frequency (wavelength) and the two coordinates on the observation screen; one running along the grating lines and the other orthogonal to the lines, thus making for a four-dimensional pattern. This pattern can be rendered in slices along the two coordinates, which physically can be achieved by recording the sideband radiation signal along the respective observation slits.

We consider a Gaussian probe pulse, which has a duration  $\tau_p \sim 1$  ps, an electric field amplitude  $E_{p0}$ , and a Gaussian transverse profile with the beam radius  $r_p$ , which is greater than the pump beam radius,  $r_p \gg R$ . Accordingly, the instantaneous Rabi frequency associated with one of the mentioned Ar transitions (labeled j) varies in time and along the grating lines (the z coordinate) as  $\Omega_j(z,t) = \Omega_{0j} \exp[-(z^2/r_p^2 + t^2/\tau_p^2)]$ , with the maximum value of  $\Omega_{0j} = (\mu_{ab})_j E_{p0}/\hbar$ . Thus, for each available sideband frequency value  $\Omega_j < \Omega_{0j}$  the emission occurs at the elliptic line  $z^2/r_p^2 + t^2/\tau_p^2 = \ln(\Omega_{0j}/\Omega_j)$  in the (zt) coordinates. The spectra of the blueshifted (+) and redshifted (-) sidebands of an emitter occupying the position z along the nth line of the excitation grating and associated with the jth transition (the  $(z, x_n)$  emitter of the jth kind) are then obtained by the

Fourier transform as

$$\mu_{j\pm}(\omega, z, x_n) = -\frac{(\mu_{ab})_j}{2} \int_{-\infty}^{\infty} dt \frac{\Omega_j(t)}{\Omega'_j(t, z)} \left[ \frac{\Delta_j}{\Omega'_j(t, z)} \pm 1 \right] \times \exp\left[ i(\omega_c - \omega)t \pm i \int_0^t dt' \Omega'_j(t', z) \right]. \tag{11}$$

To obtain the spectral amplitude at a point on the observation screen positioned at a large distance  $y_0$  from the grating, we use the Fourier optics technique [45]. To indicate the observation point, we consider the Cartesian coordinate axes  $\tilde{x}$ 

and  $\tilde{z}$  in the plane of the observation screen to be parallel to the respective x and z axes in the grating plane, with the reference point at the axis of the probe beam (for the sake of simplicity, we assume  $y_0 \gg \tilde{z}$ , z,  $x_n$  and  $\tilde{x} \gg x_n$ ), The phase increment between an effective point emitter with coordinates  $(z, x_n)$  and the point  $(\tilde{z}, \tilde{x})$  on the observation screen for the spectral component  $\omega$  is expressed as  $(\omega/c)\sqrt{y_0^2+(\tilde{z}-z)^2+(\tilde{x}-x_n)^2}$ . Then, the amplitude of this  $\omega$  component at the point  $(\tilde{z}, \tilde{x})$  is obtained as a sum of the contributions from all of the distributed emitters. This makes for the power spectrum of the Rabi sidebands as observed at the point  $(\tilde{z}, \tilde{x})$  of the observation screen:

$$I(\omega, \tilde{x}, \tilde{z}) = \frac{\omega^4}{32\pi^2 \varepsilon_0 c^3} \left| \sum_{n,j} A_n \int_{-\infty}^{\infty} dz \frac{\mu_j(\omega, z, x_n) \exp\left[i\frac{\omega}{c}\sqrt{y_0^2 + (\tilde{z} - z)^2 + (\tilde{x} - x_n)^2}\right]}{\sqrt{y_0^2 + (\tilde{z} - z)^2 + (\tilde{x} - x_n)^2}} \right|^2, \tag{12}$$

where the expression for  $\mu_j(\omega, z, x_n)$  is given by Eq. (11) and the coefficients  $A_n$  stand for the excited-atom concentration in the *n*th grating line.

Spatial-spectral interference patterns generated numerically on the basis of Eq. (12) with the excited-atom concentrations  $A_n$  determined by the calculations of Sec. III are presented in Fig. 3, where the five panels correspond to the five excitation gratings presented in Fig. 2. The probe 800 nm pulse is of  $3 \times 10^9 \,\mathrm{W/cm^2}$  intensity and  $\tau_p = 1 \,\mathrm{ps}$ duration, with the probe beam radius  $r_p = 50 \,\mu\text{m}$ . The distance between the grating and the observation screen is  $y_0 =$ 20 cm; the observation slit runs along the  $\tilde{x}$  axis (orthogonal to the grating lines) at a distance  $\tilde{z} = 2.8 \,\mathrm{cm}$  from the center. The vertical axis in the panels is the wavelength (in nm), and the horizontal axis is the  $\tilde{x}$  coordinate on the screen (in cm). The observed complex spotty patterns are due to the discussed spectral and spatial interference of the sideband radiation emitted from the grating. The isolated bright spots result from the constructive spatial interference between the Rabi sideband radiation emitted by different grating lines. The grouping of these spots in parallel curved rows is due to the spectral interference and the contribution from the sidebands related to the five Ar transitions engaged. The curved shape of these rows is determined by the spatial profile of the probe beam. The overall spatial-spectral pattern comprises multiple-order bright spots at the wavelengths shifted about the carrier wavelength of the probe pulse.

A comparison of the patterns presented in the five panels of Fig. 3 reveals their sensitivity to the phase delay  $\varphi$  between the grating-generating pump pulses. At  $\varphi=0$ , when the excitation grating contains one central maximum with two equally pronounced weaker secondary maxima [Fig. 2(a)], the Rabi sideband radiation from these secondary maxima is too feeble to interfere considerably with the radiation from the central maximum. Consequently, the observed signal is almost entirely contributed by the central maximum only. Hence, the spatial-spectral pattern consists of parallel curved continuous strips, as would be the case for a single plasma

channel [see Fig. 3(a)]. When the value of interbeam phase delay is increased to  $\varphi = \pi/4$ , the excited-atom concentration in one of the secondary maxima increases, while that in the other decreases. Now, the Rabi sideband radiation from this enhanced secondary maximum is able to interfere more assertively with the radiation from the central maximum. As a result, bright spots (which indicate the spatial interference) emerge on the background of the curved parallel strips in Fig. 3(b). Further increase in the interbeam phase delay to  $\varphi =$  $\pi/2$  leads to further enhancement of one secondary maximum at the expense of the virtual disappearance of the other. Due to considerable spatial interference between the waves emitted by the main and the secondary maxima, the spatial-spectral pattern now contains distinct bright spots studded on vague curved lines, Fig. 3(c). When interbeam phase delay becomes  $\varphi = 3\pi/4$ , the excited-atom concentration in the secondary maximum becomes nearly equal to that in the central maximum, which yields distinct bright spots with a diminishing curved line structure, Fig. 3(d). Eventually, at the interbeam phase delay of  $\varphi = \pi$ , the concentrations in the two maxima become equal, producing isolated bright spots as indicative of the dominant spatial interference, Fig. 3(e). The observed trend is quantified as the variation of the spot contrast, which is defined as Contrast % =  $100\% \times (I_{\text{spot}} - I_{\text{line}})/I_{\text{spot}}$ , where  $I_{\rm spot}$  is the signal intensity at the central bright spot and  $I_{\rm line}$ is the intensity midway between this spot and the next one in the row. The dependence of the contrast on the phase delay between the two pump pulses is presented in Fig. 3(f). When  $\varphi = 0$ , the contrast is very low. As  $\varphi$  increases, the contrast between the spots and the line also increases. At  $\varphi = \pi$ , the contrast eventually becomes 100%, which indicates complete disappearance of the connecting line due to strong destructive spatial interference.

This evolution of the spatial-spectral pattern showcases the control that the interbeam phase delay of the gratinggenerating pump pulses exerts on the eventual structure of the Rabi sideband emission from the spatially modulated filament wake channel.

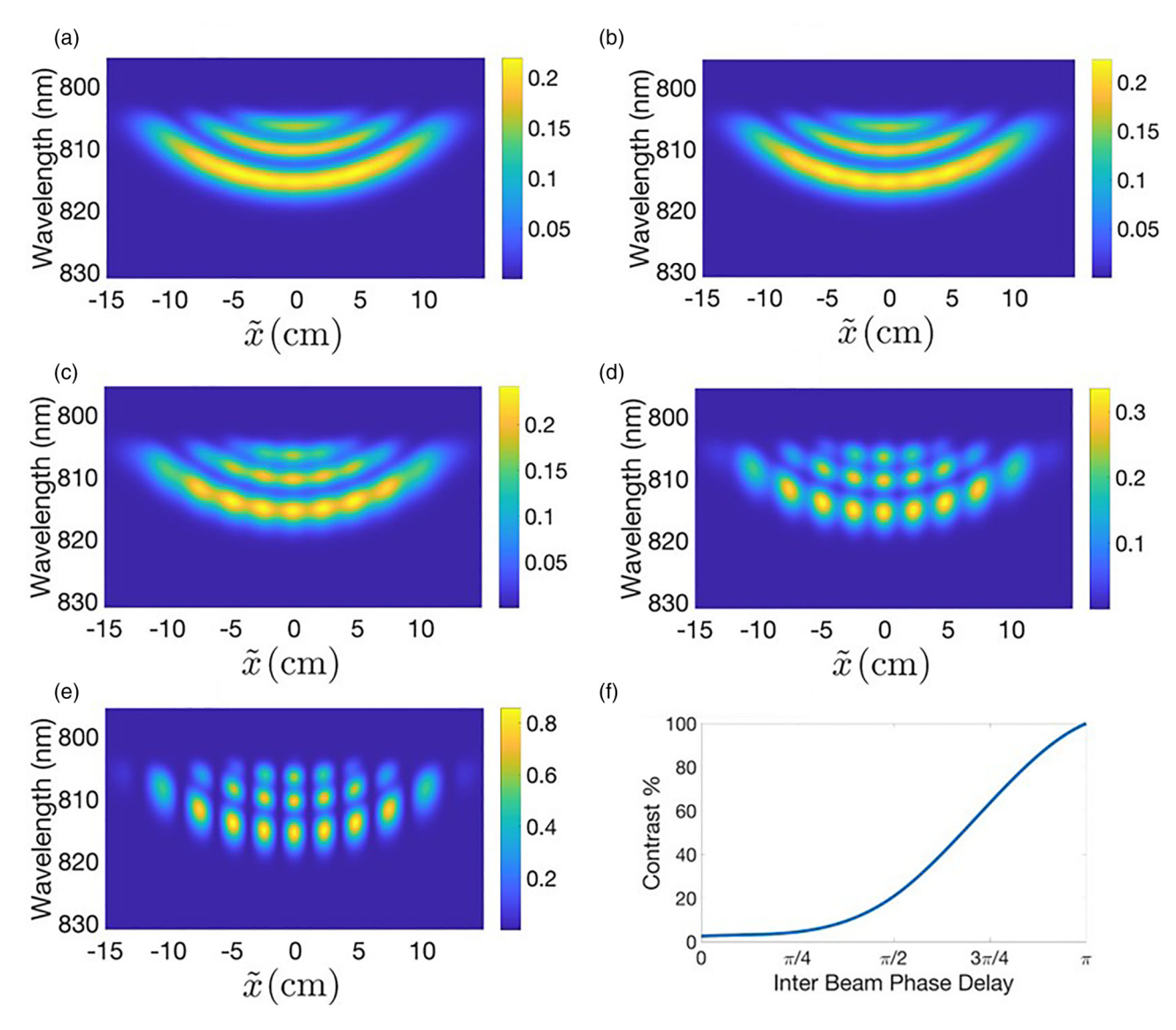


FIG. 3. Rabi sidebands at fixed distance  $y_0 = 20\,\mathrm{cm}$  to the observation screen. The pump-beam crossing angle  $\theta = 0.057\,\mathrm{rad}$ ; the phase delay between the pump pulses is (a)  $\varphi = 0$ ; (b)  $\varphi = \pi/4$ ; (c)  $\varphi = \pi/2$ ; (d)  $\varphi = 3\pi/4$ ; (e)  $\varphi = \pi$ . (These are the same parameters as those of the gratings in the respective panels of Fig. 2.) Panel (f) shows the change of the bright-spot contrast with the increase in the phase delay between the pump pulses.

## V. CONCLUSIONS

We have considered femtosecond laser filamentation caused by a transient intensity grating in a crossing area of two laser beams in a dense argon gas and have shown that the electron-collisional processes during the laser pulse lead to formation of a controllable finite grating of excited-atom density that is left in the pulse wake. The positions and magnitude of the maximum-density lines in this finite grating are effectively controlled by the phase delay between the femtosecond pulses in the crossing beams. The control effect is manifested in modifications of the spatial-spectral interference patterns of the Rabi sidebands emitted from the grating.

The Rabi sideband emission serves as a hallmark of the massive presence and distribution of excited Ar atoms in the wake channel. The excited state of Ar that forms the excitation grating can participate in five optical transitions with the wavelengths conveniently close to the standard 800 nm

of a Ti:sapphire laser. These transitions in the excited states manifold couple effectively with a picosecond probe laser pulse, resulting in emission of Rabi sidebands at frequencies redshifted and blueshifted about the laser carrier frequency and having characteristic fringe patterns determined by the spectral interference.

We calculated the distribution of the sideband spectral intensity over a remote observation screen, when the picosecond probe pulse impinges normally on the excitation grating and generates a multicomponent Rabi sideband radiation of considerable spectral complexity. The amplitude of the generated field depends on the excited-atom density distribution in the grating, while the extent of the Rabi frequency's spatial variation is determined by the transverse profile of the probe beam. Then, the emitted radiation is involved in spatial and spectral interference and produces complicated interference patterns available for remote detection. The detected signal intensity depends on the wavelength and on two spatial coordinates

(along the grating lines and perpendicular to them), thus making for a four-dimensional spatial-spectral interference pattern. We considered a three-dimensional cut of this pattern obtained with an observation slit perpendicular to the grating lines, and we traced the variations of the recorded pattern in response to changes in the phase delay between the crossing pump pulses that generate the transient excitation grating.

The predicted generation of finite excitation gratings in dense gases at the crossing of two laser beams allows for producing these gratings at desired positions in the gas and with desired controllable characteristics, including the grating separation, the length of the grating lines, and the variations of excited-atom density along the grating lines and from line to line. These characteristics can be observable in experiment, as imprinted in the spatial-spectral interference patterns of the Rabi sideband emission from the grating. Further, the contrast variations across these patterns can be indicative of the concurrent free-electron-density gratings that affect the

decoherence processes [43]. Thus, the proposed approach can serve both for production of transversely structured filament wake channels and for independent, spatially resolved diagnostics of these channels. In a more distant prospect, the generation of the broad Rabi sidebands and spatially resolved control of their spectral structure open possibilities for creating sources of coherent radiation that can be controlled toward spatially selective quasi-frequency-comb structures [33]. The results obtained on the control of transient optical nonlinearities in filament wake channels warrant experimental verification.

### ACKNOWLEDGMENT

This work was supported by the National Science Foundation under Grant No. PHY1806594 and by the Office of Naval Research under Award No. N00014-15-1-2574.

- [1] L. Bergé, S. Skupin, R. Nuter, J. Kasparian, and J. P. Wolf, Ultrashort filaments of light in weakly ionized, optically transparent media, Rep. Prog. Phys. **70**, 1633 (2007).
- [2] A. Couairon and A. Mysyrowicz, Femtosecond filamentation in transparent media, Phys. Rep. **441**, 47 (2007).
- [3] S. L. Chin, Femtosecond Laser Filamentation, Springer Series on Atomic, Optical, and Plasma Physics Vol. 55 (Springer, Berlin, 2010).
- [4] S. L. Chin, T. J. Wang, C. Marceau, J. Wu, J. S. Liu, O. Kosareva, N. Panov, Y. P. Chen, J. F. Daigle, S. Yuan, A. Azarm, W. W. Liu, T. Seideman, H. P. Zeng, M. Richardson, R. Li, and Z. Z. Xu, Advances in intense femtosecond laser filamentation in air, Laser Phys. 22, 1 (2012).
- [5] A. Filin, R. Compton, D. A. Romanov, and R. J. Levis, Impact-Ionization Cooling in Laser-Induced Plasma Filaments, Phys. Rev. Lett. 102, 155004 (2009).
- [6] D. A. Romanov, R. Compton, A. Filin, and R. J. Levis, Dynamics of strong-field laser-induced microplasma formation in noble gases, Phys. Rev. A 81, 033403 (2010).
- [7] J. H. Odhner, D. A. Romanov, and R. J. Levis, Self-shortening Dynamics Measured Along a Femtosecond Laser Filament in Air, Phys. Rev. Lett. 105, 125001 (2010).
- [8] X. H. Gao, G. Patwardhan, S. Schrauth, D. W. Zhu, T. Popmintchev, H. C. Kapteyn, M. M. Murnane, D. A. Romanov, R. J. Levis, and A. L. Gaeta, Picosecond ionization dynamics in femtosecond filaments at high pressures, Phys. Rev. A 95, 013412 (2017).
- [9] T. D. Grow, A. A. Ishaaya, L. T. Vuong, and A. L. Gaeta, Collapse and Stability of Necklace Beams in Kerr Media, Phys. Rev. Lett. 99, 133902 (2007).
- [10] H. Mishina and T. Asakura, Two Gaussian beam interference, Nouv. Rev. Opt. 5, 101 (1974).
- [11] J. Knoester and S. Mukamel, Transient gratings, 4-wave mixing, and polariton effects in nonlinear optics, Phys. Rep. 205, 1 (1991).
- [12] J. Y. Bigot, M. A. Mycek, S. Weiss, R. G. Ulbrich, and D. S. Chemla, Instantaneous Frequency Dynamics of Coherent Wave

- Mixing in Semiconductor Quantum Wells, Phys. Rev. Lett. **70**, 3307 (1993).
- [13] D. Romanov, A. Filin, R. Compton, and R. Levis, Phase matching in femtosecond BOXCARS, Opt. Lett. 32, 3161 (2007).
- [14] L. Plaja and L. Roso, Analytical description of a plasma diffraction grating induced by two crossed laser beams, Phys. Rev. E 56, 7142 (1997).
- [15] Z. M. Sheng, J. Zhang, and D. Umstadter, Plasma density gratings induced by intersecting laser pulses in underdense plasmas, Appl. Phys. B: Lasers Opt. **77**, 673 (2003).
- [16] L. L. Yu, Z. M. Sheng, and J. Zhang, Plasma Bragg density gratings produced by optical-field ionization, J. Opt. Soc. Am. B 26, 2095 (2009).
- [17] S. Suntsov, D. Abdollahpour, D. G. Papazoglou, and S. Tzortzakis, Femtosecond laser induced plasma diffraction gratings in air as photonic devices for high intensity laser applications, Appl. Phys. Lett. 94, 251104 (2009).
- [18] J. K. Wahlstrand and H. M. Milchberg, Effect of a plasma grating on pump-probe experiments near the ionization threshold in gases, Opt. Lett. **36**, 3822 (2011).
- [19] J. H. Odhner, D. A. Romanov, E. T. McCole, J. K. Wahlstrand, H. M. Milchberg, and R. J. Levis, Ionization-Grating-Induced Nonlinear Phase Accumulation in Spectrally Resolved Transient Birefringence Measurements at 400 nm, Phys. Rev. Lett. 109, 065003 (2012).
- [20] L. P. Shi, W. X. Li, Y. D. Wang, X. Lu, L. E. Ding, and H. P. Zeng, Generation of High-Density Electrons Based on Plasma Grating Induced Bragg Diffraction in Air, Phys. Rev. Lett. 107, 095004 (2011).
- [21] Y. Liu, M. Durand, S. Chen, A. Houard, B. Prade, B. Forestier, and A. Mysyrowicz, Energy Exchange between Femtosecond Laser Filaments in Air, Phys. Rev. Lett. 105, 055003 (2010).
- [22] M. Durand, Y. Liu, B. Forestier, A. Houard, and A. Mysyrowicz, Experimental observation of a traveling plasma grating formed by two crossing filaments in gases, Appl. Phys. Lett. 98, 121110 (2011).

- [23] M. Durand, A. Jarnac, Y. Liu, B. Prade, A. Houard, V. Tikhonchuk, and A. Mysyrowicz, Dynamics of plasma gratings in atomic and molecular gases, Phys. Rev. E 86, 036405 (2012).
- [24] H. Peng, C. Riconda, M. Grech, C. T. Zhou, and S. Weber, Dynamical aspects of plasma gratings driven by a static ponderomotive potential, Plasma Phys. Controlled Fusion 62, 115015 (2020).
- [25] L. Lancia, J. R. Marques, J. Fuchs, M. Nakatsutsumi, A. Mancic, P. Antici, C. Riconda, S. Weber, V. T. Tikhonchuk, A. Heron, S. Huller, J. C. Adam, and P. Audebert, Experimental investigation of identical wavelength short light pulses crossing in underdense plasma, in *Conference on Harnessing Relativistic Plasma Waves as Novel Radiation Sources From Terahertz to X-Rays and Beyond*, Proceedings Vol. 7359 (SPIE, Bellingham, WA, 2009).
- [26] G. Lehmann and K. H. Spatschek, Laser-driven plasma photonic crystals for high-power lasers, Phys. Plasmas 24, 056701 (2017).
- [27] H. Peng, C. Riconda, S. Weber, C. T. Zhou, and S. C. Ruan, Frequency Conversion of Lasers in a Dynamic Plasma Grating, Phys. Rev. Appl. 15, 054053 (2021).
- [28] D. A. Romanov, X. H. Gao, A. L. Gaeta, and R. J. Levis, Intrapulse impact processes in dense-gas femtosecond laser filamentation, Phys. Rev. A 97, 063411 (2018).
- [29] S. Bajpai and D. A. Romanov, Control of the excited-to-ionized atoms ratio in a dense gas in the wake of an intense femtosecond laser pulse, Phys. Rev. E 105, 045210 (2022).
- [30] R. Compton, A. Filin, D. A. Romanov, and R. J. Levis, Observation of Broadband Time-Dependent Rabi Shifting in Microplasmas, Phys. Rev. Lett. 103, 205001 (2009).
- [31] R. Compton, A. Filin, D. A. Romanov, and R. J. Levis, Dynamic Rabi sidebands in laser-generated microplasmas: Tunability and control, Phys. Rev. A 83, 053423 (2011).
- [32] G. Heck, R. Compton, A. Filin, M. Plewicki, D. A. Romanov, and R. J. Levis, Spatial-spectral distribution of Rabi radiation generated in plasma, Opt. Lett. 36, 3224 (2011).

- [33] D. A. Romanov, A. I. Filin, and R. J. Levis, Control of spectral interference patterns in broad Rabi sidebands toward quasicomb structures, Opt. Lett. 40, 717 (2015).
- [34] D. A. Romanov and R. J. Levis, Delayed ionization and excitation dynamics in a filament wake channel in a dense-gas medium, Phys. Rev. A 102, 013110 (2020).
- [35] L. R. Peterson and J. E. Allen, Electron-impact cross-sections for argon, J. Chem. Phys. **56**, 6068 (1972).
- [36] S.-F. Zhao, A.-T. Le, C. Jin, X. Wang, and C. D. Lin, Analytical model for calibrating laser intensity in strong-field-ionization experiments, Phys. Rev. A 93, 023413 (2016).
- [37] H. Zimmermann, S. Patchkovskii, M. Ivanov, and U. Eichmann, Unified Time and Frequency Picture of Ultrafast Atomic Excitation in Strong Laser Fields, Phys. Rev. Lett. 118, 013003 (2017).
- [38] M. V. Ammosov, N. B. Delone, and V. P. Krainov, Tunnel ionization of complex atoms and atomic ions in alternating electromagnetic field, Zh. Eksp. Teor. Fiz. 91, 2008 (1986) [Sov. Phys. JETP 64, 1191 (1986)].
- [39] W. Lotz, An empirical formula for electron-impact ionization cross-section, Z. Angew. Phys. 206, 205 (1967).
- [40] Y. P. Raizer, Laser-Induced Discharge Phenomena (Consultants Bureau, New York, 1977).
- [41] E. Gargioni and B. Grosswendt, Electron scattering from argon: Data evaluation and consistency, Rev. Mod. Phys. 80, 451 (2008).
- [42] J. E. Sansonetti, W. C. Martin, and S. L. Young, Handbook of Basic Atomic Spectroscopic Data (version 1.1.2) (National Institute of Standards and Technology, Gaithersburg, MD, 2005), http://physics.nist.gov/Handbook.
- [43] G. Heck, A. Filin, D. A. Romanov, and R. J. Levis, Decoherence of Rabi oscillations in laser-generated microplasmas, Phys. Rev. A 87, 023419 (2013).
- [44] M. Plewicki, R. Compton, A. Filin, D. A. Romanov, and R. J. Levis, Origin of the spectral coherence in dynamically broadened Rabi sidebands, Opt. Lett. 35, 778 (2010).
- [45] J. W. Goodman, *Fourier Optics*, 3rd ed. (Roberts & Company, Greenwood Village, CO, 2003).